# Effects of frustration on the nonequilibrium dynamics of photoexcited lattice systems

Nikolaj Bittner,[1,*] Denis Golež,[2,3] Martin Eckstein,[4] and Philipp Werner[1,†]
[1]*Department of Physics, University of Fribourg, 1700 Fribourg, Switzerland*
[2]*Flatiron Institute, Simons Foundation, 162 Fifth Avenue, New York, New York 10010, USA*
[3]*Jožef Stefan Institute, Jamova 39, SI-1000, Ljubljana, Slovenia*
[4]*Department of Physics, University of Erlangen-Nürnberg, 91058 Erlangen, Germany*

(Received 24 May 2020; revised 7 December 2020; accepted 15 December 2020; published 31 December 2020)

We theoretically investigate the effects of spin frustration on the nonequilibrium dynamics of photoexcited carriers in a half-filled two-dimensional Hubbard model. Using a nonequilibrium generalization of the dynamical cluster approximation, we compare the relaxation dynamics in lattices which interpolate between the triangular lattice and square lattice configuration. To clarify the influence of the density of states of the different lattices, we also consider the corresponding single-site dynamical mean-field theory results. Our study shows that the cooling effect resulting from the disordering of the spin background is less effective in the triangular case because of the frustration. This manifests itself in a longer relaxation time of the photodoped population, as measured by the time-resolved photoemission signal, and a higher effective temperature of the photodoped carriers in the nonthermal steady state after the intra-Hubbard-band thermalization.

DOI: 10.1103/PhysRevB.102.235169

## I. INTRODUCTION

Rich physics can be expected in systems which combine strongly correlated electrons and effects of frustration due to the lattice geometry [1–4]. This is the result of an inability of the system to minimize simultaneously all the interactions. A good illustration is an electron system with antiferromagnetic interactions on a two-dimensional triangular lattice. Placing two electrons on a triangle with antiparallel spin orientations makes it impossible for the third one to form two antiferromagnetic bonds. Hence, frustrated lattice systems typically exhibit not only asymmetric electron bands, due to the broken particle-hole symmetry, but also a large manifold of highly degenerate states associated with the spin frustration, and may therefore be highly susceptible to external perturbations.

A potential playground for studying frustrated systems are cold atoms in optical lattices, where all parameters can be adjusted independently. Recent advances in cooling procedures have enabled simulations of the two-dimensional (2D) Hubbard model and the observation of antiferromagnetic order [5], the structure of the chemically doped states [6], as well as anomalous transport [7] at elevated temperatures. This progress may soon enable the study of exotic phases of matter, like quantum spin liquid (QSL) states, that exhibit a variety of new features associated with their topological character [8]. Moreover, recently several solids have been proposed to host QSL states, including organic materials [9–14], quantum kagome lattices [15–17], and other triangular systems like 1T-$TaS_2$ [18,19]. While the low-temperature properties of frustrated materials have been investigated for decades, much less is known about the effect of frustration on their nonequilibrium dynamics [20,21]. In view of the nontrivial underlying physics, it is interesting to identify the fingerprints of frustration in nonequilibrium probes. Here, it may be necessary to distinguish the spin frustration from effects related to the density of states (DoS), which can also affect the nonequilibrium dynamics of the system.

An established approach for studying the properties of a strongly correlated electron system out of equilibrium is the nonequilibrium implementation [22] of dynamical mean field theory (DMFT) [23,24]. This method is able to describe the different electronic structures which arise from the different lattice configurations. However, it accounts for nonlocal correlations and interactions only at the mean field level, which is not sufficient to capture the effects of spin frustration. Extensions of DMFT, such as extended DMFT (EDMFT) [25–27] or the combination of GW and EDMFT [28,29], were successfully used in nonequilibrium settings [30,31], and in particular enabled to study the dynamical screening associated with nonlocal interactions [30].

While the EDMFT scheme employed in Ref. [32] can describe the effect of short-range spin correlations, standard DMFT and GW + DMFT do not capture the coupled dynamics of electron and spin fluctuations, which is important for the nonequilibrium description of frustrated systems. For the purpose of this work, extensions of the DMFT approach which explicitly treat the short-range correlations within a small cluster are therefore more suitable [33,34]. These cluster-based extensions have been extensively used in the equilibrium context and have already provided useful insights into the properties of the Hubbard model on a triangular lattice [35–37]. Implementations of cluster-based DMFT methods for out-of-equilibrium problems are however still rare and

*nikolaj.bittner@unifr.ch
†philipp.werner@unifr.ch

 

nonequilibrium studies of nonlocal correlation effects represent a frontier in this research field [38–41].

In the present work, we reveal possible fingerprints of spin frustration in photodoped Mott insulating systems. The photoexcitation of electrons across a large Mott gap leads to the creation of long-lived doublon (holon) type charge carriers in the upper (lower) Hubbard band. For a fixed density of photoexcited charge carriers, we investigate how their dynamics and quasi-steady-states are influenced by frustration. Specifically, we explore this question within Mott insulating Hubbard models on different two-dimensional (2D) lattices configurations at half filling, using a nonequilibrium generalization of the dynamical cluster approximation (DCA) [33,34]. When comparing the relaxation dynamics for different lattices, one must take into account that in addition to the spin frustration, the systems may have qualitatively different electronic structures. In particular, the square lattice is particle-hole symmetric, while the triangular lattice is not. In order to rule out an important effect of the asymmetric bands on the nonequilibrium dynamics, we compare the DCA results to single-site DMFT simulations. The latter approach does not properly describe nonlocal spin correlations but captures the differences in the relaxation which arise from the different electronic structures.

Because the ordering temperature in the frustrated system can be expected to be much lower than in the unfrustrated system, we consider systems without long-range magnetic order but treat the short-range spin correlations within the clusters. This allows us to characterize the effect of frustration already in the disordered state without the need for realizing long-range order. On nonfrustrated lattices, the doublons and holons can efficiently dissipate their kinetic energy by reducing the short-range spin correlations that are present even above the Néel temperature. Spin frustration leads to a less effective spin cooling in the triangular case, compared to a square lattice geometry. We demonstrate this effect by analyzing the time-dependent spin correlation functions and the photoemission spectrum. Slow relaxation times of doublons and holons and their hot energy distributions in the nonthermal steady states are nonequilibrium fingerprints of spin frustration.

The paper is organized as follows. Section II describes the model and observables. Section III presents the results of our study for electronic systems with spin frustration in and out of equilibrium, while Sec. IV summarizes the main findings.

## II. MODEL AND METHOD

We consider a half-filled Hubbard model on a triangular lattice with anisotropic hopping parameters, which is described by the time-dependent Hamiltonian

$$\hat{H}(t) = -\sum_{\langle i,j\rangle\sigma}(t_{i,j}(t)\hat{c}^{+}_{i\sigma}\hat{c}_{j\sigma} + \text{H.c.}) - \mu\sum_{i}\hat{n}_i + U\sum_{i}\hat{n}_{i\uparrow}\hat{n}_{i\downarrow}. \quad (1)$$

Here $\hat{c}^{(+)}_{i,\sigma}$ annihilates (creates) an electron on lattice site $i$ with spin $\sigma$ and $\langle i, j\rangle$ represent pairs of nearest-neighbor sites. The

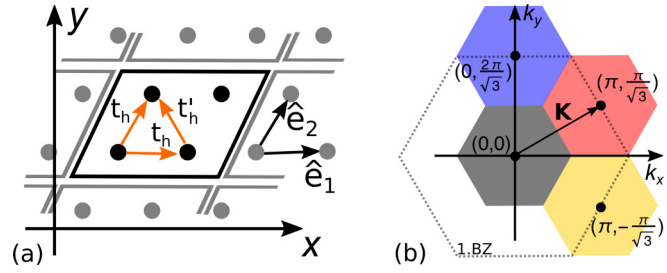


FIG. 1. (a) Illustration of the triangular lattice in real space and of the direction-dependent electron hoppings. A real-space cluster with $N_c = 2 \times 2$ sites is marked by the black line. (b) Corresponding reciprocal space representation with $N_c$ cells. The coarse graining around the momentum points **K** in the first Brillouin zone (1. BZ) is indicated by the colored areas.

density operator is $\hat{n}_i = \hat{n}_{i\uparrow} + \hat{n}_{i\downarrow}$ with $\hat{n}_{i,\sigma} = \hat{c}^{+}_{i,\sigma}\hat{c}_{i,\sigma}$, $U$ is the onsite interaction parameter, and $\mu$ the chemical potential. The hopping is direction dependent and takes the form [see Fig. 1(a)]:

$$t_{i,j}(t) = \begin{cases} t_h(t) & \text{along } \hat{e}_1, \hat{e}_2 \\ t'_h & \text{along } \hat{e}_2 - \hat{e}_1 \end{cases}, \quad (2)$$

where $t'_h$ varies from the unfrustrated limit $t'_h = 0$ (distorted square lattice) to the fully frustrated triangular case with $t'_h = t_h$. The bare dispersion $\epsilon_{\mathbf{k}}$ for the system with direction-dependent hopping parameters takes the form

$$\epsilon_{\mathbf{k}} = -2\Big[t_h\cos(k_x) + t_h\cos\Big(\frac{1}{2}k_x + \frac{\sqrt{3}}{2}k_y\Big) + t'_h\cos\Big(\frac{1}{2}k_x - \frac{\sqrt{3}}{2}k_y\Big)\Big]. \quad (3)$$

We note that the bandwidth $W$ of the noninteracting system depends on the degree of the frustration, namely $W = 8t_h$ for $t'_h = 0$ and $W = 9t_h$ for $t'_h = t_h$.

In order to study the relaxation dynamics of photodoped doublons and holons in Mott insulating systems described by Eq. (1), we employ the nonequilibrium generalization of the dynamical cluster approximation (DCA) in combination with a noncrossing approximation (NCA) impurity solver [41–43]. Within this formalism, the cluster reference system (without bath) is represented by the cluster Hamiltonian

$$H^c(t) = -\sum_{\langle i,j\rangle\sigma}\big[t^c_{i,j}(t)\hat{d}^{+}_{i\sigma}\hat{d}_{j\sigma} + \text{H.c.}\big] - \mu\sum_{i}\hat{n}_i + U\sum_{i}\hat{n}_{i\uparrow}\hat{n}_{i\downarrow}, \quad (4)$$

with $\hat{d}^{(+)}_{i\sigma}$ denoting the annihilation (creation) operators on the cluster. The cluster hopping parameters $t^c_{i,j}$ ($t^c_{i,j} = 6t_{i,j}/\pi^2$) are renormalized by the averaging over momentum patches in the DCA method, which also imposes translation invariance on the cluster. All the sites of this cluster are hybridized with a self-consistently determined bath. In this work, we use a $2 \times 2$ cluster, which corresponds to $N_c = 4$ patches in

reciprocal space (see Fig. 1) around the momentum points $\mathbf{K} = \{(0,0), (\pi, \pi/\sqrt{3}), (\pi, -\pi/\sqrt{3}), (0, 2\pi/\sqrt{3})\}$ [35,37,44].

The photodoping of the large-gap Mott insulating state is generated by a time-dependent modulation of the hopping parameter along the $\hat{e}_1$ and $\hat{e}_2$ directions (see Fig. 1):

$$t_h(t) = t_h^0 + \Delta t_h e^{-(t-t_0)^2/\tau^2} \sin(\Omega_p(t-t_0)), \tag{5}$$

with amplitude $\Delta t_h$. The hopping modulation has a Gaussian envelope with a maximum at time $t_0$ and a full width at half maximum $\tau$. The excitation frequency $\Omega_p$ is chosen according to the gap size and the bandwidth. We measure the energy in units of the hopping $t_h^0$ of the unfrustrated system and time in units of $\hbar/t_h^0$. This excitation protocol is chosen because treating electric fields in the DCA formalism (which enforces translation invariance on the cluster) within a gauge-invariant formulation is not straightforward [45]. In an experiment, one could choose to selectively modulate the hopping parameter $t_h$ along the $\hat{e}_1$ and $\hat{e}_2$ directions, if the polarization is perpendicular to the direction of the $t_h'$ bond, or affect all three bonds. Such excitations can be directly implemented in cold atom experiments and also in solid state systems by driving an IR-active phonon mode coupled to the intersite hopping. However, the details of the excitation protocol should not be of qualitative importance for our results: The effect of the excitation protocol is to generate a broad distribution of nonequilibrium carriers by an almost impulsive perturbation, while the main focus of this study is on the relaxation of carriers after the excitation. We have checked that an additional temporal modulation of $t_h'$ does not qualitatively change the results.

### A. Observables

In this section, we define the observables that will be used to analyze the properties of these 2D lattice systems in and out of equilibrium. Whereas the single-particle observables are equivalent on the lattice and on the cluster, we measure the two-particle observables only on the cluster to avoid the computationally challenging solution of Bethe-Salpeter equations. The cluster results, e.g., for the spin correlations, may not be identical to the lattice observables, but we expect them to reproduce the qualitative trends [34].

#### *1. Double occupation*

The double occupancy (or doublon density) $D(t)$ is defined as

$$D(t) = \frac{1}{N_c} \sum_{i=1}^{N_c} \langle \hat{n}_{i\uparrow}(t) \hat{n}_{i\downarrow}(t) \rangle \tag{6}$$

with $i$ labeling the cluster sites. Within the DCA formalism, it is convenient to measure $D(t)$ in momentum space, as discussed in Ref. [41].

#### *2. Spin-spin correlation function*

To measure the short-range spin correlations we calculate the nearest neighbor (NN) spin-spin correlation function on the $2 \times 2$ cluster. For the relevant cases of the fully frustrated triangular system ($t_h' = t_h$) and the tilted square lattice ($t_h' = 0$), we define the spin-spin correlation function as

$$S_{\mathrm{NN}}(t) = \frac{1}{N_\delta} \sum_{\langle i,j \rangle} \langle \hat{S}_i^z(t) \hat{S}_j^z(t) \rangle \tag{7}$$

with $\hat{S}_i^z$ denoting the spin operator in the $z$ direction at site $i$ and $N_\delta$ the number of pairs of neighboring sites connected by $t_h$, see also Ref. [39]. Taking into account the periodicity of the cluster, the spin frustrated system has $N_\delta = 12$, while the tilted square lattice has $N_\delta = 8$.

#### *3. Spectral functions*

To calculate the equilibrium spectral functions, we perform the Fourier transformation of the retarded component of the local Green's function:

$$A(\omega) = -\frac{1}{\pi} \mathrm{Im} \int_0^{t_{\max}} dt e^{-i\omega t} G^R(t) \tag{8}$$

with the Fourier time window $t_{\max} = 10$ and $G^R = 1/N_c \sum_{\mathbf{K}} G^R_{\mathbf{K}}$. Here, $G_{\mathbf{K}}(t,t') = -i\langle d_{\mathbf{K}}(t) d^+_{\mathbf{K}}(t') \rangle$ is the cluster Green's function, and $G^R$ denotes the retarded part. We analyze the relaxation dynamics of the photodoped population by computing the nonequilibrium photoemission spectrum [46]

$$I(\omega, t_p) = -\mathrm{Im} \int d\bar{t} d\bar{t}' e^{-i\omega(\bar{t}-\bar{t}')} G^<(t_p + \bar{t}, t_p + \bar{t}') \times S(\bar{t}) S(\bar{t}'), \tag{9}$$

where $S(t) \propto \exp[-(t^2/(2\Delta t^2_{\mathrm{probe}})]$ is the envelope of the probe pulse of length $\Delta t_{\mathrm{probe}} = 1.5$, and $G^<$ the lesser component of the Green's function.

## III. RESULTS

### A. Equilibrium properties

In this section we discuss equilibrium properties of the half-filled 2D Hubbard models with different lattice geometries. The temperature of the system is set to $T = 0.1$, unless otherwise specified, and we focus on the paramagnetic Mott phase.

#### *1. Double occupancy*

The $U$ dependence of the double occupancy $D_{\mathrm{eq}}$ [Eq. (6)] in equilibrium is plotted in Fig. 2(a) for a square lattice (green dashed line with squares), tilted square lattice (triangular lattice with $t_h' = 0$, green solid line with diamonds), and triangular lattice with $t_h' = t_h$ (red solid line with triangles). To take into account the different bandwidths $W$ of the electronic systems, we normalize the horizontal axis by $W$. The temperature $T = 0.1$ is above the critical endpoint of the Mott transition, which occurs around $U/W \sim 1$ for the triangular lattice [2,3,37] and $U/W \sim 0.5$ for the square lattice [37,39]. On all lattices, the double occupancies $D_{\mathrm{eq}}$ are decreasing with increasing interaction $U$, however, there are quantitative differences between the lattices.

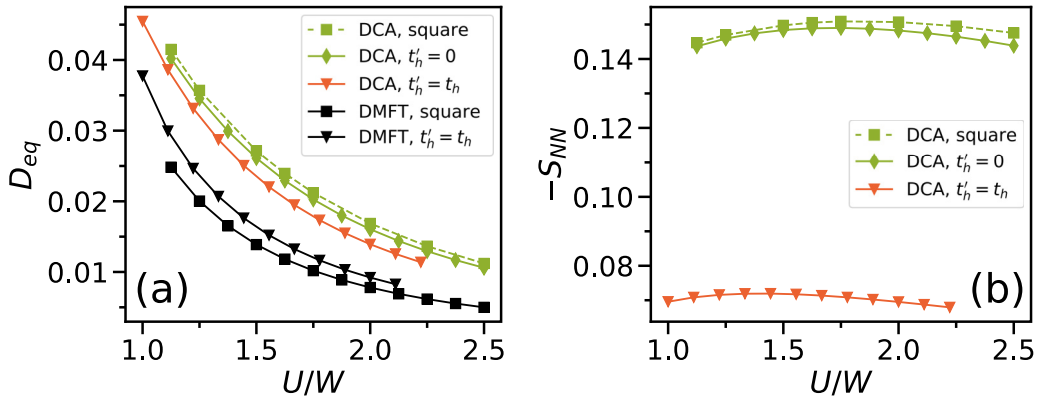


FIG. 2. (a) Double occupancy calculated at $T = 0.1$ using DCA for different lattice geometries: the tilted square lattice ($t_h' = 0$, solid green line with diamonds), the square lattice (dashed green line with squares), and the triangular lattice ($t_h' = t_h$, solid red line with triangles). For comparison, we also show results from DMFT calculations at the same temperature for the square (black line with squares) and triangular lattice (black line with triangles). The horizontal axis is normalized by the noninteracting bandwidth $W$. (b) Corresponding nearest neighbor spin-spin correlation function calculated using DCA with the same color coding as in panel (a).

First, we compare the results for the square lattice with those for the tilted square lattice (triangular lattice with $t_h' = 0$). These two cases actually correspond to the same lattice Hamiltonian. The slight discrepancy in the results originates from averaging over different patches in the Brillouin zone (square-shaped patches centered at $\mathbf{K} = \{(0,0), (\pi,0), (0,\pi), (\pi,\pi)\}$ versus hexagonal patches centered at $\mathbf{K} = \{(0,0), (\pi,\pi/\sqrt{3}), (\pi,-\pi/\sqrt{3}), (0,2\pi/\sqrt{3})\}$), and therefore quantifies a DCA coarse graining error. In the fully frustrated triangular system with $t_h' = t_h$ the double occupancy is suppressed compared to the square lattice case. This can be explained by the effect of the spin frustration, which suppresses antiferromagnetic spin correlations and thus increases the Pauli blocking of virtual hopping processes which contribute to $D_{\mathrm{eq}}$. This effect will be further confirmed by analyzing the spin-spin correlation functions in the following subsection.

It is also interesting to compare the DCA double occupancies within the corresponding single-site DMFT results, plotted by black lines in Fig. 2(a). We see that in the latter case the double occupancy is reduced. This can be explained by the fact that in contrast to DMFT, the DCA simulation captures nonlocal antiferromagnetic spin correlations, which reduce the Pauli blocking effect. Hence, nonlocal correlations have also a significant effect on local observables, such as the double occupation. We further notice that the effect of $t_h'$ on $D_{\mathrm{eq}}$ is not correctly captured by single-site DMFT, which only takes into account the effect of $t_h'$ on the density of states but misses the effect of frustration.

#### 2. Short range spin correlations

The frustration picture is confirmed by analyzing the nearest-neighbor spin-spin correlations, see Eq. (7). The equilibrium results obtained using the DCA approximation are plotted in Fig. 2(b) as a function of $U/W$ for the square lattice, tilted square lattice ($t_h' = 0$), and triangular lattice ($t_h' = t_h$). In contrast, single-site DMFT does not capture the effect of short-range correlations on the electrons.

Again, we see that the spin-spin correlation functions are very similar on the square lattice and the tilted square lattice, and the small numerical differences originate from the different patch geometries. However, in the triangular lattice case ($t_h' = t_h$) the spin-spin correlations in the $z$ direction are suppressed by about a factor of two due to the effect of spin frustration in the presence of antiferromagnetic nearest-neighbor correlations.

#### 3. Spectral function

In Fig. 3(a), we plot the equilibrium spectral functions [see Eq. (8)] obtained using the DCA approximation for several lattice configurations: the square lattice (green dashed line), the tilted square lattice ($t_h' = 0$, green solid line), and the triangular lattice ($t_h' = t_h$, red solid line). In order to eliminate effects associated with carrier recombination after the photoexcitation (discussed in Sec. III B), we choose the value of the interaction strength $U$ such that the corresponding Mott gap is almost twice as large as the bandwidth. Comparing $A(\omega)$ for the square and the tilted square lattice we see that the results are in good agreement: (i) both calculations yield almost the same value of the Mott gap ($\Delta_{\mathrm{Mott}} \approx 15$), and (ii) the symmetric Hubbard bands (with width $W \approx 8.2$) exhibit a similar two-peak structure. However, the details differ between the two spectra due to the averaging over different patches.

Including $t_h' = t_h$ leads to a smaller value of the Mott gap and to asymmetric Hubbard bands, due to the lack of particle-hole symmetry in the triangular lattice. The latter is illustrated in the inset of Fig. 3(b) which shows the corresponding noninteracting DoS. The frustrated lattice configuration also results in different bandwidths of the lower Hubbard band ($W_{\mathrm{LHB}} \approx 8.6$) and upper Hubbard band ($W_{\mathrm{UHB}} \approx 7.9$). For a meaningful comparison between the models, we adjust the interactions $U$ in the models with $t_h' > 0$ in such a way that the spectral functions roughly reproduce the gap size of the model with $t_h' = 0$. Additionally, for a

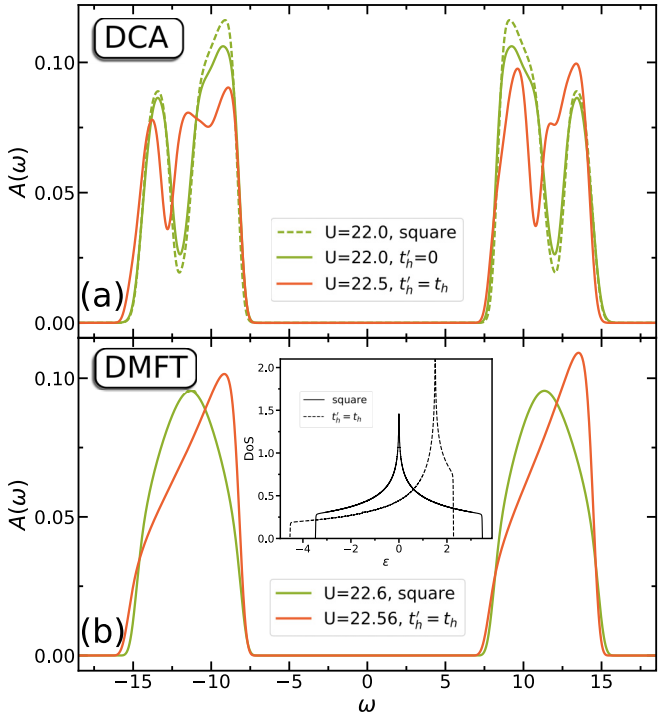


FIG. 3. Equilibrium spectral functions for different lattice geometries obtained using (a) the DCA and (b) the DMFT approximation. The interaction strengths $U$ and the hopping parameters $t_h$ have been adjusted to roughly match the gap size and the band width. (a) Spectral function for a tilted square lattice with $t_h' = 0$, $U = 22$ (solid green line) and a triangular lattice (solid red line) with renormalized parameters ($t_h' = t_h \to 0.8t_h^0$, $U = 22.5$). For comparison, we also plot the spectral function for a square lattice with $U = 22$ (dashed green line). (b) DMFT spectral function for the square lattice (green solid line) with the renormalized parameters ($t_h \to 0.87t_h^0$, $U = 22.6$) and for the triangular lattice (red solid line) with renormalized parameters ($t_h' = t_h \to 0.76t_h^0$, $U = 22.56$). The inset shows the noninteracting DoS for the corresponding square and triangular lattices, respectively.

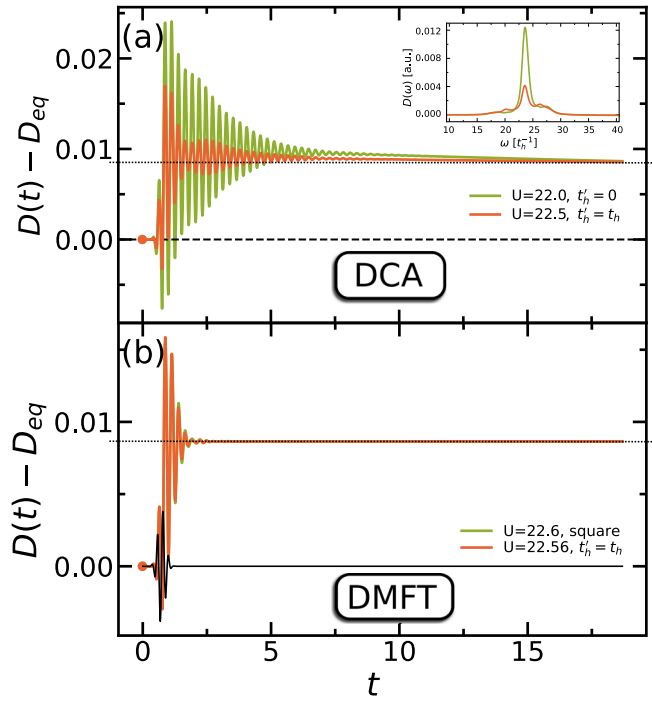


FIG. 4. Pulse-induced change in the double occupation. The parameters of the Mott-Hubbard systems are the same as in the equilibrium calculations (see Fig. 3). (a) The DCA evolution of the double occupancy after a short excitation for the tilted square lattice (green line) and the triangular lattice (red line). The inset shows the Fourier transform of the data directly after pumping (with a smooth background subtracted) to illustrate the oscillations with a frequency $\omega \approx U$. (b) The DMFT evolution for the double occupancy on the square lattice (green line) and on a triangular lattice (red line). The excitation strength is chosen such that the same photodoping is achieved for the longest propagation time, namely $\Delta t_h \approx 0.4$ for the tilted square lattice and $\Delta t_h \approx 0.47$ for the triangular lattice in the DCA case. The excitation strengths in the DMFT case are $\Delta t_h \approx 0.55$ and $\Delta t_h \approx 0.45$ for the square and triangular lattices, respectively. The black line in (b) represents the pulse $(t_h(t) - t_h^0)$ in arbitrary units. Horizontal dotted lines in (a) and (b) serve as a guide to the eye.

given degree of frustration $t_h' > 0$ the hopping parameter $t_h$ is renormalized with respect to its counterpart for the square lattice ($t_h \to \alpha t_h^0$ with a scaling factor $\alpha$) in order to roughly match the bandwidths of the models. Due to the asymmetry of the Hubbard bands in the triangular case, the resulting LHB is thus slightly broader than its counterpart for the square lattice, while the width of the upper Hubbard band is reduced by a corresponding amount. As an illustration, we plot in Fig. 3 the spectral function of the Hubbard model in the triangular case with the renormalized hopping parameters $t_h' = t_h \to 0.8t_h^0$ (red solid line).

We complement the DCA discussion by analyzing the single-site DMFT results, see Fig. 3(b). Again, for a meaningful comparison between different models, we adjust the interactions $U$ and hopping parameters $t_h$ in order to reproduce the gaps and bandwidths of the spectral functions obtained using DCA. While the asymmetry (symmetry) between the UHB and the LHB for the triangular (square) lattice is captured by the DMFT spectrum, the fine structure of the Hubbard bands is different. The fine structure is influenced by short-range correlations, whereas the splitting of the Hubbard bands into subbands is likely to be overemphasized in the four-site DCA, as a result of the coarse discretization of the self-energy in momentum space. In the following nonequilibrium analysis, we will fix the parameters for each lattice as discussed in this section and only vary the parameters of the hopping modulation [Eq. (5)].

### B. Nonequilibrium properties

A hopping modulation of the form (5) with appropriate frequency creates charge excitations across the Mott gap. For the parameters of the photoexcitation we use a pulse with $\Omega_p = 29$ centered at $t_0 \approx 0.73$, with a full width at half maximum $\tau = 0.2$ (the pulse lasts up to $t \approx 1.8$, see Fig. 4). Here, we are interested in the relaxation dynamics of the photoinduced

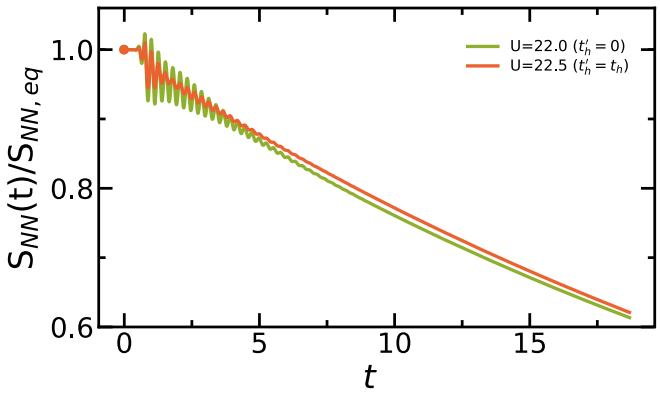


FIG. 5. Nearest-neighbor spin-spin correlation function (normalized by its equilibrium value) for a tilted square lattice (solid green line) and a triangular lattice (solid red line). The excitation protocols are the same as in Fig. 4(a).

doublons within the UHB, which results from electron-electron scattering and interactions with the spin background. To end up with a given density of photoinduced doublons for the different lattice geometries, we adjust the intensity of the photoexcitation accordingly. The dynamics is then analyzed by means of the time-dependent observables introduced in Sec. II A.

#### *1. Double occupancy*

First, we compare the time-dependent double occupancy during and after the photodoping pulse in the tilted square lattice ($t_h' = 0$) and the triangular lattice ($t_h' = t_h$). The nonequilibrium DCA results are shown by the green and red solid lines in Fig. 4(a), respectively. The excitation intensity in these calculations has been adjusted in such a way that the increase in the long-lived doublons, measured at the longest accessible time, is approximately the same in both models, $D(t = 18.7) - D_{\rm eq} \approx 0.01$. The corresponding pulse amplitudes are $\Delta t_h = 0.4$ and $\approx 0.47$ for the square and the triangular lattices, respectively.

Because of the large Mott gap, the lifetime of the photodoped doublons and holons is much longer than the maximum simulation time [43], so that their density is almost conserved at $t \gtrsim 10$. In the DCA case, there is however a small difference in the lifetime of the doublons on the square and triangular lattices. One possible reason could be the effect of spin correlations. In the square-lattice model with strong antiferromagnetic correlations the system can convert the energy released by a doublon-holon recombination process into spin excitations [47]. However, the doublon lifetime scales exponentially with the gap size [48,49], and rough estimates suggest a decay rate which is much smaller than observed in Fig. 4(a). A more plausible explanation rests on the observation that the small decaying component evolves on a timescale comparable to the dynamics of the spin correlations (see Fig. 5). $D(t)$ measures both the number of excited charge carriers and a contribution from virtual quantum fluctuations which dress the Mott state. Due to the Pauli exclusion principle, these fluctuations are possible only on a bond with antiferromagnetic nearest neighbor correlations, as explained in Sec. III A 1. Therefore the double occupancy $D(t)$ contains a small decaying component proportional to the nearest neighbor spin correlations, which is larger for the square lattice, compared to the triangular lattice.

Further evidence for the role of spin correlations is found in the time evolution after the pulse. The photoexcitation of the system lasts only up to $t \approx 1.8$ [see black curve in Fig. 4(b)]. However, in $D(t) - D_{\rm eq}$ we observe strong photoinduced oscillations with a frequency $\approx U$ [see inset in Fig. 4(a)] superimposed on an almost step-function-like increase. These oscillations originate from hoppings of electrons to nearest neighbors and back, similar to virtual fluctuations. With increasing frustration (increasing value of $t_h'$), the amplitude of these fluctuations is reduced, since the reduced antiferromagnetic nearest-neighbor correlations enhance the Pauli blocking. The latter effect also explains why a larger pulse strength is needed in the frustrated lattice to produce the same doublon density as in the square lattice.

For comparison, we also performed nonequilibrium single-site DMFT calculations for the square and triangular lattice, where we again adjusted the density of the long-lived photoinduced doublons to approximately the same value. The single-site DMFT results in Fig. 4(b) show a very rapid suppression of the oscillations in $D(t)$ after the end of the pump pulse and an almost identical dynamics for the square and triangular lattice geometry. Since single-site DMFT does not capture short-range spin correlations, and the oscillations are controlled by $U$, this result is expected and shows that details of the DoS have little effect on the doublon production and damping behavior. By comparing the single-site DMFT with the DCA results one can conclude that spin frustration, via its effect on the short-range spin correlations and the Pauli blocking, has a significant impact on the doublon dynamics after a short pulse excitation and in particular leads to a strong damping of the $\omega \approx U$ oscillations.

#### *2. Short-range spin correlations*

While the density of doublons and holons is essentially conserved after the pulse, the spin-spin correlations decrease monotonically with increasing time (see Fig. 5), apart from small oscillations associated with the previously mentioned nearest-neighbor hopping processes. To compare the dynamics in the models with $t_h' = 0$ and $t_h' = t_h$, we normalize the values of $S_{\rm NN}(t)$ by the equilibrium value, which makes it clear that the decay rate is approximately independent of the degree of frustration. This is consistent with the picture of spin disorder resulting from the hopping of doublons and holons in the initially correlated spin background, assuming that the hopping rate is approximately the same for both values of $t_h'$.

Qualitatively similar results were previously obtained and discussed in Ref. [39] for the case of a square lattice. The decay of the spin-spin correlation function implies a transfer of (kinetic) energy to the spin sector, which is directly detectable in the time evolution of the doublon distribution function as shown in the following subsection. Since in absolute values $S_{\rm NN}(t)$ is about a factor of two larger in the square lattice compared to the triangular counterpart [c.f. Fig. 2(b)], this means that the amount of energy transferred to the spin sector

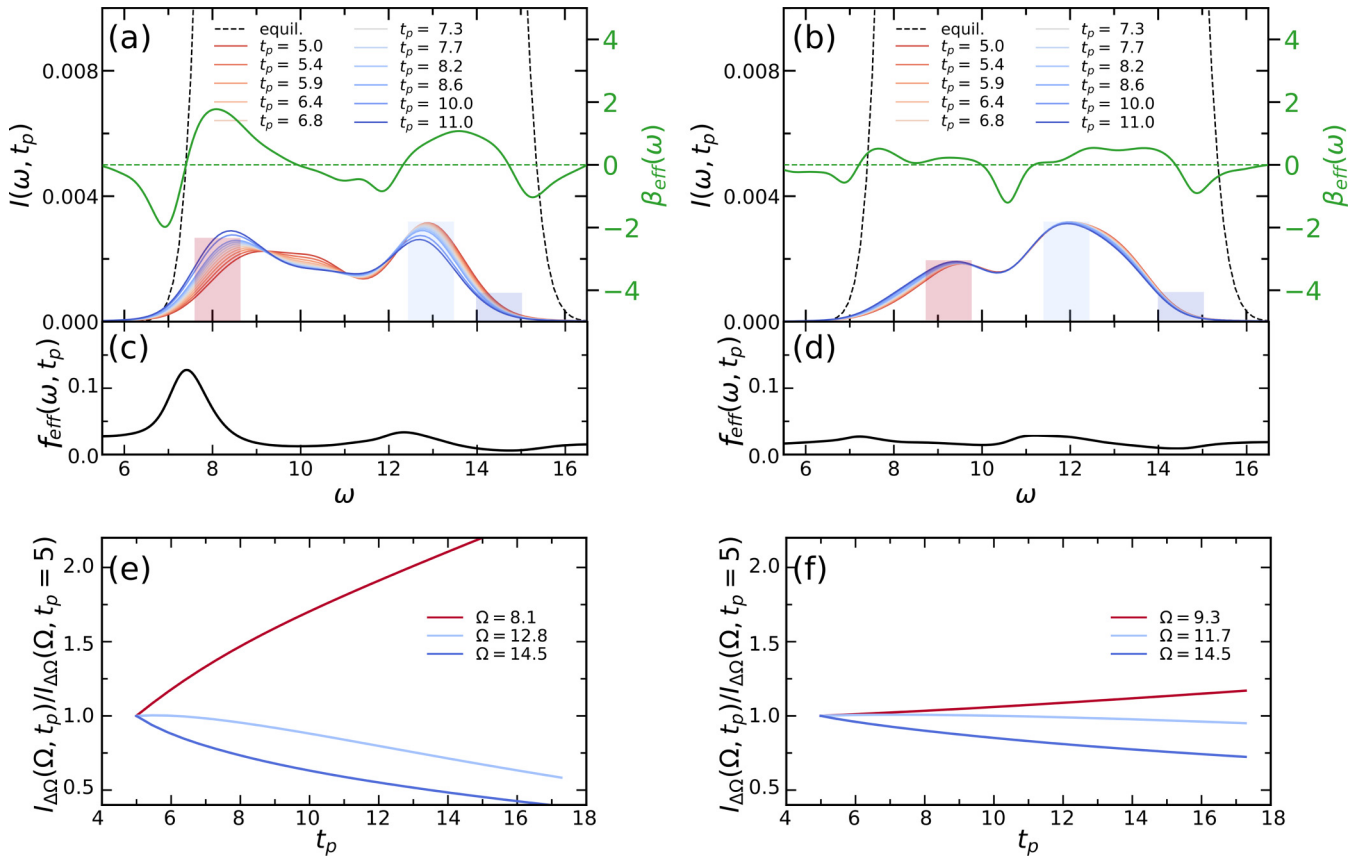


FIG. 6. (a),(b) Occupation in the upper Hubbard band for a tilted square lattice with $t_h' = 0$ (left) and for a triangular lattice with $t_h' = t_h$ (right) after photodoping (colored solid lines) obtained using the DCA approximation. The black dashed line corresponds to the spectral function calculated from the retarded component of the Green's function in equilibrium, whereas the green solid line corresponds to the effective inverse temperature $\beta_{\text{eff}}$ calculated at $t_p \approx 11$. (c),(d) Effective distribution function calculated at $t_p \approx 11$. (e),(f) Time-dependent photoemission spectrum integrated in the frequency window $[\Omega - \Delta\Omega, \Omega + \Delta\Omega]$ [shown by shaded areas in (a),(b) with $\Delta\Omega = 0.5$] and normalized to the value at time $t_p = 5$ for a tilted square lattice and a triangular lattice, respectively.

(for fixed photodoping concentration) is larger in the square lattice case. We thus anticipate a more effective spin cooling in the square lattice compared to the triangular lattice.

### 3. *Nonequilibrium spectral functions*

In this section, we calculate nonequilibrium spectral functions [Eq. (9)] in the energy range of the UHB, which provides information about the relaxation dynamics of the photoexcited charge carriers, the energy dissipation to the spin background, and its dependence on spin frustration. These simulations and analyses represent the main result of our study. In particular, in Figs. 6(a) and 6(b) we plot $I(\omega, t_p)$ for several times after the excitation (which lasts up to $t \approx 1.8$). The left panel corresponds to the tilted square lattice, whereas the right panel shows the result for the triangular lattice with $t_h' = t_h$. The frequency of the excitation pulse is chosen in such a way that the short pulse generates a broad and rather uniform occupation in the UHB with a peak closer to its upper edge. After the pulse the corresponding spectral weight is redistributed within the UHB as shown in Figs. 6(a) and 6(b) by the colored solid lines. To analyze more quantitatively the redistribution of the spectral weight within the Hubbard band, we integrate the nonequilibrium spectral function in frequency windows of width $2\Delta\Omega$, centered at different $\Omega$:

$$I_{\Delta\Omega}(\Omega, t_p) = \int_{\Omega-\Delta\Omega}^{\Omega+\Delta\Omega} I(\omega, t_p) d\omega. \tag{10}$$

The results are plotted in Figs. 6(c) and 6(d) for the tilted square lattice and triangular lattice, respectively. Here, the curves are normalized to the value at probe time $t_p = 5$ and we use $\Delta\Omega = 0.5$. As one can see, in both models the spectral weight is shifting towards lower frequencies, i.e., the photodoped doublons lose kinetic energy. However, the occupation transfer in the tilted square lattice is much more pronounced than in the triangular case. For example, the relative decrease of the spectral weight at the upper band edge ($\Omega = 14.5$) between $t_p = 5$ and $t_p = 14$ is about 50% in the tilted square lattice, while it is only ∼20% in the triangular lattice. Even more remarkable is the difference between the two models when we consider the relative increase in spectral weight near the lower band edge where the increase is >100% in the square lattice as compared to ∼10% in the triangular lattice. In contrast, in DMFT simulations (see Fig. 8 in the

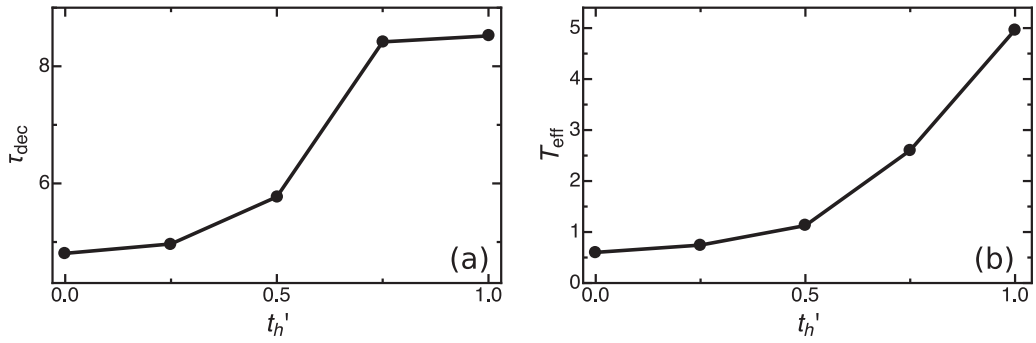


FIG. 7. (a) Relaxation time (measured in units of $t_h$) extracted from the PES spectral weight at the upper edge of the UHB as a function of the hopping parameter $t_h'$. (b) Effective temperature measured at the lower edge of the UHB at time $t \approx 11$.

Appendix), where short-range correlations do not play any significant role, the distribution of the spectral weight in the UHB hardly changes after the photo excitation for both the square and triangular lattices [49].

For a more quantitative analysis of the relaxation dynamics in systems with different degrees of frustration, we extracted the relaxation time from the time-dependent spectral weight at the upper edge of the UHB. The corresponding data are fitted in the time interval $t \in [6, 10]$ by a single exponential function of the form:

$$I_{\Delta\Omega}(t) = A + B\exp(-t/\tau_{\rm dec}), \tag{11}$$

where $A$ and $B$ are fitting parameters and $\tau_{\rm dec}$ is the relaxation time. The results are plotted in Fig. 7(a) as a function of the hopping parameter $t_h'$ (degree of frustration). As one can see, increasing frustration leads to a monotonous increase of the relaxation time, which almost doubles for $t_h' = t_h$ compared to the case with $t_h' = 0$. This is consistent with the observation in Sec. III B 2, where it was shown that the amount of energy transferred to the spin background is about a factor of two lower in the triangular lattice compared to the square lattice. The longer relaxation time in the triangular lattice hence illustrates the reduced coupling between the charge and spin degrees of freedom in the frustrated system and the resulting less effective spin cooling. A significant effect of the different DoS can again be ruled out by comparing with the single-site DMFT simulations (see Fig. 8), where we find almost no difference between the relaxation dynamics of the doublons in the square and triangular lattices.

Looking back at Fig. 4 we notice that the effect of $t_h'$ on the relaxation of the spectral weight $I_{\Delta\Omega}(t)$ is opposite to the effect on the damping of the oscillations in the double occupation $D(t)$. This is no contradiction because the latter oscillations are averaged out in the measurement of $I_{\Delta\Omega}$ due to the width of the probe pulse $\Delta t_{\rm probe} \gg \frac{2\pi}{U}$. On average, $D(t)$ is conserved after the photodoping, up to small drifts related to modifications in the virtual hopping contribution. The oscillations shown in Fig. 4 represent a hopping of electrons back-and-forth between neighboring sites, which happens on top of an overall relaxation in the kinetic energy of the doublon population. This hopping is damped more strongly in the triangular lattice case because of enhanced Pauli blocking. The overall relaxation of the doublon population towards the lower edge of the UHB, measured by $I_{\Delta\Omega}(t)$, is however slower in a spin-frustrated lattice [Fig. 7(a)], because it is controlled by the dissipation of kinetic energy to the spin background.

#### *4. Effective temperature*

To characterize the nonthermal steady state after the photoexcitation, we calculate the effective temperature from the fluctuation-dissipation theorem [40,50]

$$h(\omega, t_p) = \log[-{\rm Im}G^R(\omega, t_p)/{\rm Im}G^<(\omega, t_p) - 1] \tag{12}$$

with $G^R$ and $G^<$ denoting the retarded and lesser components of the nonequilibrium Green's function. The Fourier time window for the calculation of $G^R(\omega, t_p)$ and $G^<(\omega, t_p)$ [analogous to Eq. (8) for fixed $t_p$] is set to 10. The slope of $h(\omega, t_p)$ defines a frequency-dependent effective inverse temperature $\beta_{\rm eff} = 1/T_{\rm eff}$. The results measured at $t \approx 11$ for the tilted square and triangular lattice are shown by the solid green line in Figs. 6(a) and 6(b), respectively. As one can see, $\beta_{\rm eff}(\omega)$ shows a strong $\omega$ dependence and even sign changes, especially in the region of the "pseudogap" in $A(\omega)$ (which may be overestimated in DCA due to the piece-wise constant self-energy in momentum space). This implies that on the short timescales of this simulation, the system has not yet thermalized very well, and the distribution function is not a Fermi function with a single temperature over the whole energy range. This is also directly seen by the distribution function $f_{\rm eff}(\omega, t_p) = {\rm Im}G^<(\omega, t_p)/{\rm Im}G^R(\omega, t_p)$, as shown in panels (c) and (d) of Fig. 6 for $t_p = 11$. On the other hand, it is evident that compared to the tilted square lattice, in the triangular lattice there is a broader occupation function, a much weaker accumulation of spectral weight at the lower band edge, and correspondingly a flatter distribution function, so that a mean effective inverse temperature in the triangular lattice would be substantially lower ($T_{\rm eff}$ is higher). For a quantitative comparison, we focus on the lowest energy peak in the nonequilibrium spectral function and extract $\beta_{\rm eff}$ at the corresponding energy. The resulting $T_{\rm eff} = 1/\beta_{\rm eff}$ is plotted in Fig. 7 for different values of the hopping parameter $t_h'$ (degree of frustration in the system). As one can see, the effective temperature $T_{\rm eff}$ of the photodoped doublons increases systematically as $t_h'$ is increased. These results demonstrate that the cooling effect associated with energy transfer to the spin

background is much reduced in a spin frustrated system. This is confirmed by the DMFT simulations [see Figs. 8(a) and 8(b) in the Appendix], where the absence of spin cooling leads to an effective inverse temperature $\beta_{\text{eff}}$ close to zero or even negative, independent of the degree of frustration.

## IV. DISCUSSION AND CONCLUSIONS

In this work we investigated the effects of spin frustration on the relaxation dynamics of photodoped carriers in the paramagnetic Mott phase of half-filled two-dimensional Hubbard models. We simulated the real-time dynamics of these systems by using the nonequilibrium extension of the dynamical cluster approximation in combination with an NCA impurity solver. The use of a $2 \times 2$ cluster with variable diagonal hoppings allowed us to interpolate between the unfrustrated square lattice and fully frustrated triangular lattice limits and thus to analyze the effects of spin frustration on the short range spin correlations and time-resolved photoemission spectra. In order to rule out a significant effect of the asymmetric density of states in the frustrated case, we compared the DCA results to single-site DMFT simulations, which capture the density of states effects but not the short range correlations. In the DMFT simulations the relaxation, e.g., of the double occupancy, is the same for the two lattices, which shows that the different relaxation in the square and triangular lattices is not merely a result of the different density of states but primarily due to different spin correlations.

We showed that spin frustration manifests itself in different nonequilibrium probes. On the one hand, the increased Pauli blocking in a system with suppressed antiferromagnetic spin correlations leads to suppressed oscillations in the double occupation after a photodoping pulse and a reduced energy absorption from the pulse. On the other hand, after doublons have been created with high kinetic energy (with a population centered in the upper half of the UHB) the spin frustration has a significant effect on the dissipation of kinetic energy to the spin background and hence the time evolution of the energy distribution function and effective temperature of the doublons. These can serve as fingerprints of the spin frustration in nonequilibrium studies.

The spin-charge coupling results in a relaxation of the photodoped carriers to lower energies and a simultaneous reduction in the nearest-neighbor spin correlations. Consistent with the results of Ref. [39], we found that this spin cooling of the photodoped carriers is very effective in the square lattice case. By systematically varying the hopping parameters we further showed that spin frustration has a significant effect on the dynamics, since it leads to a reduced energy dissipation at a given hopping rate. As a result, the triangular lattice system exhibits an intra-Hubbard band thermalization of the doublons at a much higher effective temperature than the square lattice system. This effect is not present in single-site DMFT simulations, where the effect of short-range spin correlations on the electrons is not captured.

Our results show that nonlocal effects, such as spin frustration, not only affect the low energy properties of correlated electron systems but also play an important role in highly excited nonequilibrium states. This highlights the need for developing computational methods for nonequilibrium systems which go beyond the local DMFT approximation.

## ACKNOWLEDGMENTS

This work was supported by ERC Consolidator Grant No. 724103 (N.B., P.W.), ERC Starting Grant No. 716648 (M.E.), and Swiss National Science Foundation Grant No. 200021-165539 (P.W.). D.G. acknowledges the support by the Slovenian Research Agency (ARRS) under Programs No. J1-2455 and No. P1-0044. The calculations have been performed on the Beo04 cluster at the University of Fribourg. The Flatiron Institute is a division of the Simons Foundation. We thank M. Imada for helpful discussions.

## APPENDIX: DMFT

For the purpose of comparison with the DCA results in Fig. 6, we show in Fig. 8 the corresponding nonequilibrium photoemission spectra [Eq. (9)] in the energy range of the UHB obtained using the single-site DMFT approximation. The left panels correspond to the case of a square lattice, whereas the right panels show the results for a triangular lattice ($t_h' = t_h$). The photoexcitation protocol is the same as discussed in Sec. III B 1 in connection with Fig. 4(b).

As one can see in Figs. 8(a) and 8(b), the photoinduced spectral weight in the UHB does not significantly change with time for both lattice geometries. This can be explained by a very fast relaxation towards a nonthermal steady state due to the lack of short-range spin correlations. The calculated inverse effective temperature $\beta_{\text{eff}}$ in this state at $t \approx 11$ (green line) shows in both cases almost frequency independent values close to zero [similar to the effective distribution function shown in panels (c) and (d)], which is also consistent with the absence of spin cooling.

To get more quantitative insights into the dynamics of the spectral weight within the UHB, we calculate the integrated spectral function $I_{\Delta\Omega}(\Omega, t_p)$ according to Eq. (10). The normalized results with respect to $I_{\Delta\Omega}(\Omega, t_p = 5)$ are plotted in Figs. 8(e) and 8(f). Whereas the system in the square lattice case shows no changes in $I_{\Delta\Omega}(\Omega, t_p)$ with probing time $t_p$, the spectral weight for the triangular lattice geometry is shifting from the lower edge of the UHB to its upper edge. We note, however, that this result is obtained from the division of two very small numbers. In absolute values the time-dependent changes are tiny.

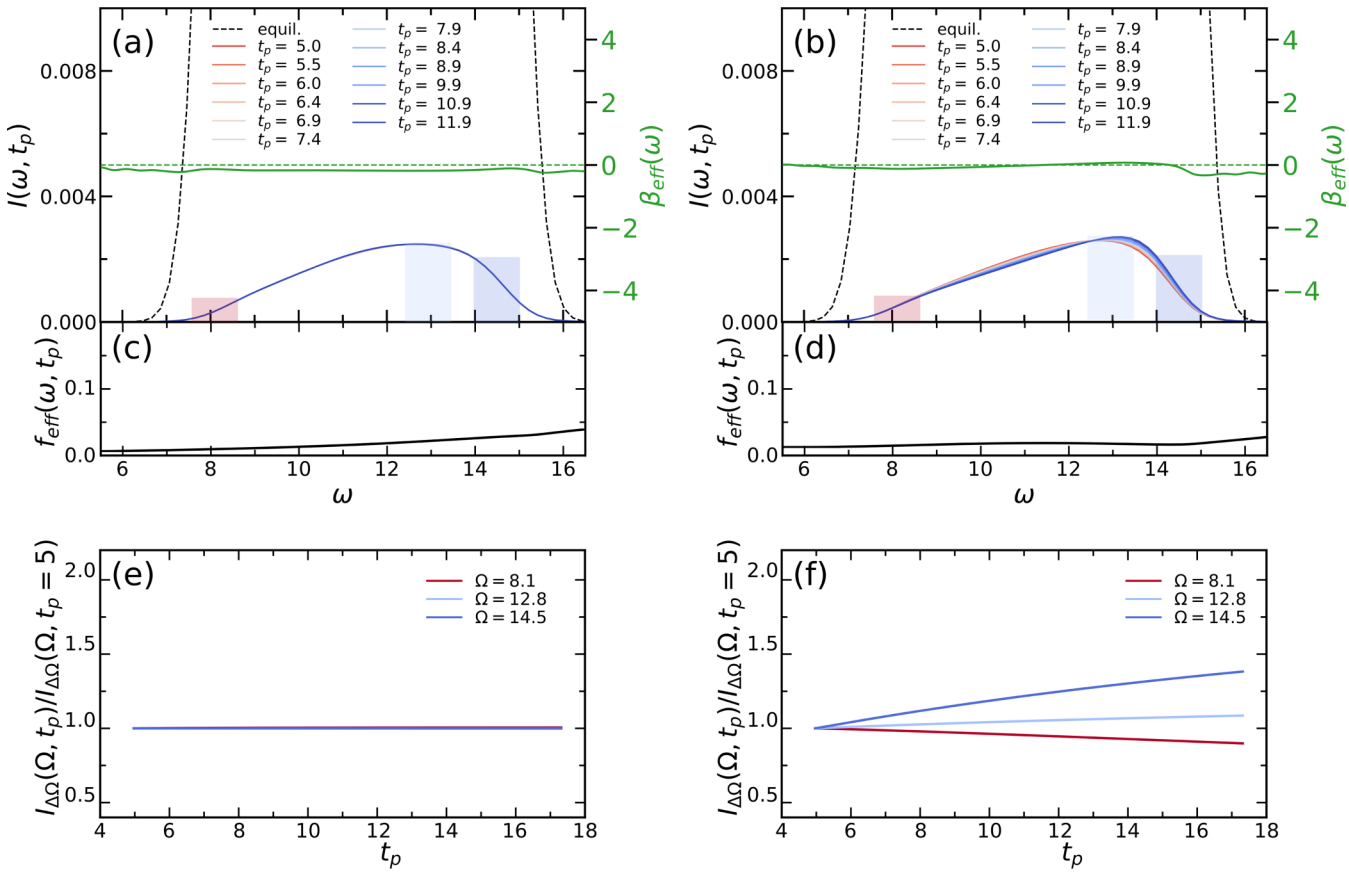


FIG. 8. (a),(b) Occupation in the upper Hubbard band for a square lattice (left) and for a triangular lattice with $t_h' = t_h$ (right) after photodoping (colored solid lines) obtained using the DMFT approximation. The black dashed line corresponds to the spectral function calculated from the retarded component of the Green's function in equilibrium, whereas the green solid line corresponds to the effective inverse temperature $\beta_{\text{eff}}$ calculated at $t_p \approx 11$. (c),(d) Effective distribution function calculated at $t_p \approx 11$. (e),(f) Time-dependent photoemission spectrum integrated in the frequency window $[\Omega - \Delta\Omega, \Omega + \Delta\Omega]$ [shown by shaded areas in (a),(b) with $\Delta\Omega = 0.5$] and normalized relative to the value at $t_p = 5$ for a square lattice and a triangular lattice, respectively. The excitation protocols are the same as in Fig. 4(b).


[1] P. Sahebsara and D. Sénéchal, Phys. Rev. Lett. **100**, 136402 (2008).

[2] T. Yoshioka, A. Koga, and N. Kawakami, Phys. Rev. Lett. **103**, 036401 (2009).

[3] T. Shirakawa, T. Tohyama, J. Kokalj, S. Sota, and S. Yunoki, Phys. Rev. B **96**, 205130 (2017).

[4] M. Ye and A. V. Chubukov, Phys. Rev. B **100**, 035135 (2019).

[5] A. Mazurenko, C. S. Chiu, G. Ji, M. F. Parsons, M. Kanász-Nagy, R. Schmidt, F. Grusdt, E. Demler, D. Greif, and M. Greiner, Nature (London) **545**, 462 (2017).

[6] T. A. Hilker, G. Salomon, F. Grusdt, A. Omran, M. Boll, E. Demler, I. Bloch, and C. Gross, Science **357**, 484 (2017).

[7] P. T. Brown, D. Mitra, E. Guardado-Sanchez, P. Schauß, S. S. Kondov, E. Khatami, T. Paiva, N. Trivedi, D. A. Huse, and W. S. Bakr, Science **357**, 1385 (2017).

[8] L. Balents, Nature (London) **464**, 199 (2010).

[9] Y. Shimizu, K. Miyagawa, K. Kanoda, M. Maesato, and G. Saito, Phys. Rev. Lett. **91**, 107001 (2003).

[10] K. Kanoda, J. Phys. Soc. Jpn. **75**, 051007 (2006).

[11] T. Itou, A. Oyamada, S. Maegawa, M. Tamura, and R. Kato, J. Phys.: Condens. Matter **19**, 145247 (2007).

[12] M. Yamashita, N. Nakata, Y. Senshu, M. Nagata, H. M. Yamamoto, R. Kato, T. Shibauchi, and Y. Matsuda, Science **328**, 1246 (2010).

[13] S. Yamashita, T. Yamamoto, Y. Nakazawa, M. Tamura, and R. Kato, Nat. Commun. **2**, 275 (2011).

[14] T. Isono, H. Kamo, A. Ueda, K. Takahashi, M. Kimata, H. Tajima, S. Tsuchiya, T. Terashima, S. Uji, and H. Mori, Phys. Rev. Lett. **112**, 177201 (2014).

[15] T.-H. Han, J. S. Helton, S. Chu, D. G. Nocera, J. A. Rodriguez-Rivera, C. Broholm, and Y. S. Lee, Nature (London) **492**, 406 (2012).

[16] M. R. Norman, Rev. Mod. Phys. **88**, 041002 (2016).

[17] M. Gomilšek, R. Žitko, M. Klanjšek, M. Pregelj, C. Baines, Y. Li, Q. Zhang, and A. Zorko, Nat. Phys. **15**, 754 (2019).

[18] M. Klanjšek, A. Zorko, J. Mravlje, Z. Jagličić, P. K. Biswas, P. Prelovšek, D. Mihailovic, D. Arčon *et al.*, Nat. Phys. **13**, 1130 (2017).

[19] W.-Y. He, X. Y. Xu, G. Chen, K. T. Law, and P. A. Lee, Phys. Rev. Lett. **121**, 046401 (2018).
[20] T. Ishikawa, Y. Sagae, Y. Naitoh, Y. Kawakami, H. Itoh, K. Yamamoto, K. Yakushi, H. Kishida, T. Sasaki, S. Ishihara, Y. Tanaka, K. Yonemitsu, and S. Iwai, Nat. Commun. **5**, 5528 (2014).
[21] Y. Kawakami, H. Itoh, K. Yonemitsu, and S. Iwai, J. Phys. B: At., Mol. Opt. Phys. **51**, 174005 (2018).
[22] H. Aoki, N. Tsuji, M. Eckstein, M. Kollar, T. Oka, and P. Werner, Rev. Mod. Phys. **86**, 779 (2014).
[23] A. Georges, G. Kotliar, W. Krauth, and M. J. Rozenberg, Rev. Mod. Phys. **68**, 13 (1996).
[24] W. Metzner and D. Vollhardt, Phys. Rev. Lett. **62**, 324 (1989).
[25] P. Sun and G. Kotliar, Phys. Rev. B **66**, 085120 (2002).
[26] T. Ayral, S. Biermann, and P. Werner, Phys. Rev. B **87**, 125149 (2013).
[27] P. Werner and M. Casula, J. Phys.: Condens. Matter **28**, 383001 (2016).
[28] S. Biermann, F. Aryasetiawan, and A. Georges, Phys. Rev. Lett. **90**, 086402 (2003).
[29] P. Werner and M. Eckstein, Struct. Dyn. **3**, 023603 (2016).
[30] D. Golež, M. Eckstein, and P. Werner, Phys. Rev. B **92**, 195123 (2015).
[31] D. Golež, L. Boehnke, H. U. R. Strand, M. Eckstein, and P. Werner, Phys. Rev. Lett. **118**, 246402 (2017).
[32] N. Bittner, D. Golež, H. U. R. Strand, M. Eckstein, and P. Werner, Phys. Rev. B **97**, 235125 (2018).
[33] M. H. Hettler, A. N. Tahvildar-Zadeh, M. Jarrell, T. Pruschke, and H. R. Krishnamurthy, Phys. Rev. B **58**, R7475 (1998).
[34] T. A. Maier, M. Jarrell, T. Pruschke, and M. H. Hettler, Rev. Mod. Phys. **77**, 1027 (2005).
[35] H. Lee, G. Li, and H. Monien, Phys. Rev. B **78**, 205117 (2008).
[36] Y.-H. Chen, W. Wu, H.-S. Tao, and W.-M. Liu, Phys. Rev. A **82**, 043625 (2010).
[37] H. T. Dang, X. Y. Xu, K.-S. Chen, Z. Y. Meng, and S. Wessel, Phys. Rev. B **91**, 155101 (2015).
[38] N. Tsuji, P. Barmettler, H. Aoki, and P. Werner, Phys. Rev. B **90**, 075117 (2014).
[39] M. Eckstein and P. Werner, Sci. Rep. **6**, 21235 (2016).
[40] A. J. Herrmann, N. Tsuji, M. Eckstein, and P. Werner, Phys. Rev. B **94**, 245114 (2016).
[41] N. Bittner, D. Golež, M. Eckstein, and P. Werner, Phys. Rev. B **101**, 085127 (2020).
[42] H. Keiter and J. C. Kimball, J. Appl. Phys. **42**, 1460 (1971).
[43] M. Eckstein and P. Werner, Phys. Rev. B **82**, 115115 (2010).
[44] Y. Imai and N. Kawakami, Phys. Rev. B **65**, 233103 (2002).
[45] N. Lin, E. Gull, and A. J. Millis, Phys. Rev. B **80**, 161105(R) (2009).
[46] J. K. Freericks, H. R. Krishnamurthy, and T. Pruschke, Phys. Rev. Lett. **102**, 136401 (2009).
[47] Z. Lenarčič and P. Prelovšek, Phys. Rev. Lett. **111**, 016401 (2013).
[48] R. Sensarma, D. Pekker, E. Altman, E. Demler, N. Strohmaier, D. Greif, R. Jördens, L. Tarruell, H. Moritz, and T. Esslinger, Phys. Rev. B **82**, 224302 (2010).
[49] M. Eckstein and P. Werner, Phys. Rev. B **84**, 035122 (2011).
[50] D. Golež, P. Werner, and M. Eckstein, Phys. Rev. B **94**, 035121 (2016).